phys. stat. sol. (a) **162**, 39 (1997)

Subject classification: 78.30.Hv; 63.20.Dj; 72.20.Fr; S6

Raman Investigation of SiC Polytypes

S. NAKASHIMA[1]) and H. HARIMA

Department of Applied Physics, Graduated School of Osaka University, Yamadaoka 1–2, Suita, Osaka 565, Japan

(Received January 31, 1997)

It has been recognized that Raman scattering spectroscopy is a powerful tool to characterize SiC crystals non-destructively. We review recent significant developments in the use of Raman scattering to study structural and electronic properties of SiC crystals. The areas to be discussed in the first part include polytype identification, evaluation of stacking disorder and ion-implantation damages, and stress evaluation. The Raman scattering by electronic transitions is discussed in the second part of this article. We concentrate on the plasmon LO-phonon coupled modes whose spectral profiles are used to evaluate the carrier concentration and mobility. Anisotropic electronic properties of α-SiC and characteristics of heavily doped crystals are discussed. Semiconductor-to-metal transition and Fano interference effect are also treated.

1. Introduction

Silicon carbide which is a wide band gap semiconductor with an indirect band structure is an attractive material for high-temperature and high-voltage power applications and optical sensors in the ultraviolet region.

It is well known that there are a large number of polytypes for the SiC crystal [1]. The SiC polytypes are uniaxial (hexagonal or rhombohedral) except for 3C-SiC. The control of the polytype during crystal growth is quite important, because the band gap energy and electrical properties are different for different polytypes. Recent development of the crystal growth and device fabrication for SiC crystals requires the polytype identification and the qualitative characterization of as-grown and also processed SiC crystals.

Raman scattering measurement is a powerful technique for the characterization of SiC, because it is non-destructive and requires no special preparation of samples. Furthermore, the Raman efficiency of this material is high because of the strong covalency of the bonding and the Raman signals are easily obtained. The Raman parameters such as intensity, width, peak frequency and polarization of Raman bands provide fruitful information on the crystal quality. Up to now, the phonon Raman scattering has been studied for various polytypes [2 to 13]. The results of these studies demonstrate that polytype identification by Raman scattering is possible. The Raman spectroscopic technique will be widely used to evaluate SiC crystals in the near future because of its usefulness.

Another advantage of the Raman scattering is its capability of characterization of electronic properties in polar semiconductors [14]. The Raman measurement can detect coupled modes of LO-phonon and plasma oscillation of free carriers whose spectral fea-

[1]) e-mail: nakashim@ap.eng.osaka-u.ac.jp

tures depend on the carrier concentration and carrier damping. This measurement does not need electrodes for the study of the electrical properties.

In this paper we review a number of recent developments in the Raman scattering work on SiC. An emphasis is placed on the practical use of the Raman scattering for the evaluation of structural and electrical properties of SiC crystals. The present paper is divided into two parts: The first part is devoted to Raman analyses of the stacking structure of polytypes, stacking disorder, strain, polytype conversion and damage in ion-implanted SiC. The second part deals with the electrical properties of n-type 4H and 6H polytypes. Raman scattering from bound and free electrons is discussed.

2. Polytype Structure of SiC and Phonon Modes

It is well known that there are a large number of SiC polytypes for which the stacking sequences of double atomic planes of Si–C along the c-direction are different. The polytypes are regarded as natural superlattices. The crystal structures of the SiC polytypes are classified into three groups; cubic (C), hexagonal (H) and rhombohedral (R) structures. The most simple polytype with the shortest period is the 3C polytype (β-type) which has a zincblende (cubic) structure. The α-type SiC crystals are represented by the number of Si–C double layers in the unit cell and the letter H or R added to specify the lattice type. The primitive unit cell of nH or $3n$R polytypes contains n formula units (Si–C). The unit cell length of the polytypes along the c-axis (corresponding to the $\langle 111 \rangle$ direction of the zincblende structure) is n times larger than that of the basic polytype (3C polytype). Accordingly, the Brillouin zone in the direction of Γ–L is reduced to $1/n$ of the basic Brillouin zone, i.e. minizone [2, 3]. The dispersion curves of the phonon modes propagating along the c-direction in higher polytypes are approximated by folded dispersion curves in the basic Brillouin zone as shown schematically in Fig. 1. This zone

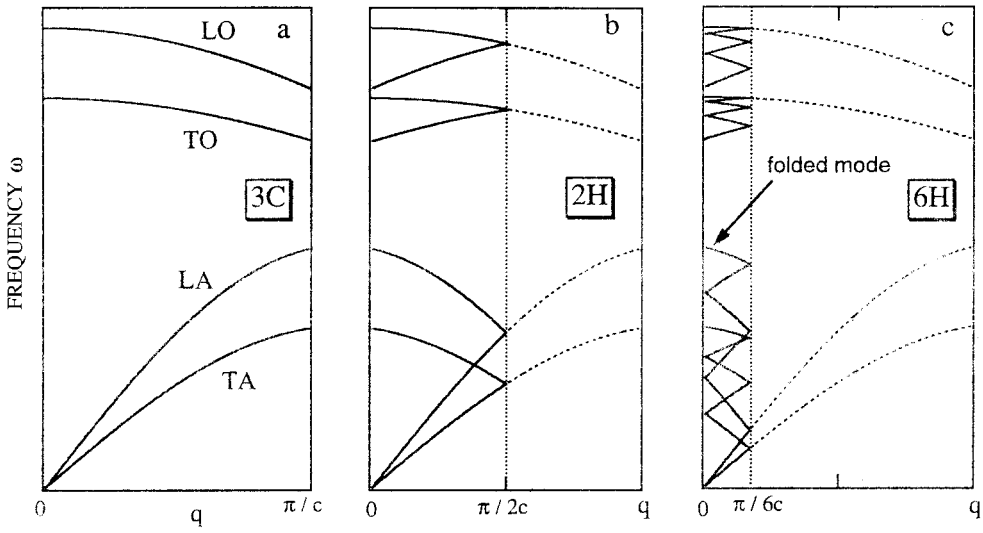

Fig. 1. Schematic phonon dispersion curves of longer period polytypes. Their dispersion curves are approximated by zone folded dispersion curves of 3C polytype. The zone folded mode at the Γ point can be observed in Raman spectra. a) 3C, b) 2H and c) 6H polytypes

folding along the [00ξ] direction provides a number of new phonon modes at the Γ point ($q = 0$) which correspond to the phonon modes inside or at the edge of the basic Brillouin zone. The phonon modes arising from the zone folding are called "folded modes".

Group theory analysis predicts a number of phonon modes at the Γ point for higher polytypes which correspond to the folded modes, because their unit cell contains a number of atoms. The unit cell of 3C-SiC contains one formula unit and there are an LO-mode and a doubly degenerate TO mode in optical branches.

Table 1

Symmetry of the folded modes at the Γ point for common polytypes. $x = q/q_B$ is the reduced wave vector of the phonon modes in the basic Brillouin zone, which corresponds to the folded modes at the Γ point. The parentheses represent acoustic modes

polytype	space group	number of atoms in the unit cell	symmetry of phonon modes				
3C	T_d^2	2	$x = (q/q_B) = 0$				
			(F_2), F_2				
2H	C_{6v}^4	4	$x = 0$	$x = 1$			
planar acoustic			(E_1)	E_2			
axial acoustic			(A_1)	B_1			
planar optic			E_1	E_2			
axial optic			A_1	B_1			
4H	C_{6v}^4	8	$x = 0$	$x = 0.5$	$x = 1$		
planar acoustic			(E_1)	$2E_2$	E_1		
axial acoustic			(A_1)	$2B_1$	A_1		
planar optic			E_1	$2E_2$	E_1		
axial optic			A_1	$2B_1$	A_1		
15R	C_{3v}^5	10	$x = 0$	$x = 0.4$	$x = 0.8$		
planar acoustic			(E)	2E	2E		
axial acoustic			(A_1)	$2A_1$	$2A_1$		
planar optic			E	2E	2E		
axial optic			A_1	$2A_1$	$2A_1$		
6H	C_{6v}^4	12	$x = 0$	$x = 0.33$	$x = 0.66$	$x = 1$	
planar acoustic			(E_1)	$2E_2$	$2E_1$	E_2	
axial acoustic			(A_1)	$2B_1$	$2A_1$	B_1	
planar optic			E_1	$2E_2$	$2E_1$	E_2	
axial optic			A_1	$2B_1$	$2A_1$	B_1	
8H	C_{6v}^4	16	$x = 0$	$x = 0.25$	$x = 0.5$	$x = 0.75$	$x = 1.0$
planar acoustic			(E_1)	$2E_2$	E_1	$2E_2$	E_1
axial acoustic			(A_1)	$2B_1$	$2A_1$	$2B_1$	A_1
planar optic			E_1	$2E_2$	$2E_1$	$2E_2$	E_1
axial optic			A_1	$2B_1$	$2A_1$	$2B_1$	A_1

For nH and $3n$R polytypes, the phonon modes with longer wavelength are divided into axial and planar modes for which atoms displace along the directions parallel and perpendicular to the c-axis, respectively. A folded mode corresponds to a phonon mode having a reduced wave vector $x = q/q_B = 2m/n$ along the $\langle 111 \rangle$ direction in the basic Brillouin zone of the 3C-SiC, where m is an integer less than or equal to $n/2$ ($m \leq n/2$) and q_B is a wave vector of the zone edge in the basic Brillouin zone. For $3n$R polytypes, the planar modes are E modes which are Raman active and the axial modes are Raman active A_1 modes. The longitudinal (transverse) phonons propagating along the c-axis belong to the A_1-type (E-type) symmetry. For nH polytypes, the planar modes consist of Raman and infrared active E_1 modes and Raman active E_2 modes, and the axial modes consist of Raman active A_1 and Raman inactive B_1 modes. Small E−A splitting occurs in the folded optic modes which propagate along the direction perpendicular to the c-axis. However, the E−A splitting for the folded acoustic modes propagating along this direction is large [2].

Table 1 shows the Ramsdell notation, space group, the number of atoms per unit cell and the symmetry of phonon modes for typical polytypes.

3. Raman Scattering Measurements

The Raman scattering is an inelastic scattering phenomenon of photons by phonons or electrons in materials. When materials are irradiated with monochromatic light, photons with energies different from that of the incident light are scattered. The scattered light is very weak and we need special spectrometers designed to eliminate strong Rayleigh light. Double or triple monochromators with gratings have widely been used to disperse the scattered light and reject stray light. The dispersed signals are detected by a photomultiplier or a multichannel detector. The multichannel detectors enable us to measure Raman lines in a wide spectral range simultaneously and then record the spectrum more rapidly compared with a single channel detector (photomultiplier).

Recently, charge coupled device (CCD) detectors have been used to detect weak signals. When using a cooled CCD detector of back illumination type, one can detect weak signals with 0.1 photon/s per pixel. More recently, exclusive spectrographs for use of the CCD detectors have been developed.

An Ar ion laser is usually used as an excitation source of the Raman scattering. α-SiC is transparent for Ar ion laser lines in the visible region. Right-angle and back scattering geometries are employed. Raman microprobe is quite useful to measure a local area of a sample [15]. When using an objective lens with a numerical aperture of NA, the diameter of the focused laser beam on a sample surface is given by

$$D = 1.22\lambda/\mathrm{NA}\,, \tag{1}$$

where λ is the wavelength of the laser light. For $\lambda = 488$ nm and NA = 0.8, we obtain $D = \approx 0.8$ μm. This implies that Raman spectra can be measured with a spatial resolution of μm or sub-μm scale. For the Raman microprobe measurement, the experimental geometry is limited to a back scattering geometry.

Since the band gap energy of α-SiC is larger than the energy of the Ar ion laser, the Raman measurement of α-SiC in the visible region is usually not disturbed by luminescence except for heavily doped samples. No special sample preparation is necessary for the Raman measurements of SiC. Surface polishing is sometimes required for measure-

ments with the back scattering geometry under a microscope in order to avoid strong light reflected from the sample surface.

The Raman bands can be observed for certain scattering geometries. For example, the back scattering geometry using the *c*-face of the α-SiC crystals allows the observation of $E(E_1)$-type TO and A_1-type LO modes. On the other hand, E_1-type LO modes are not observed for the back scattering geometry and, e.g., the right-angle scattering geometry should be used.

Precise determination of the frequency of Raman bands is necessary, especially for the measurements of LO-phonon plasmon coupled modes and stress effects. The zero-drift of Raman spectrometers with time prevents the precise frequency determination. The measured frequency is calibrated by plasma lines of the laser or emission lines of a Ne lamp.

4. Phonon Raman Spectra for SiC

4.1 Phonon dispersion curves of TA and TO modes

In Fig. 2 we will show the whole Raman spectra of 3C, 2H, 4H, 6H and 15R polytypes, which are observed with the back scattering geometry. The folded modes of transverse acoustic (FTA) and optic (FTO) branches appear intensely. As the unit cell length of the polytype is increased, the number of observable folded modes increases. For nH and $3n$R polytypes, the folded modes are classified by the reduced wave vector assigned to these modes ($x = q/q_B = 2m/n$), because the folded mode corresponds to a phonon mode at the reduced wave vector q/q_B in the Brillouin zone of the 3C polytype.

In the low frequency region below $266\,\mathrm{cm}^{-1}$, we observe sharp bands which correspond to the phonon modes in the TA branches. Doublet structures are observed for the FTA modes except for the phonon mode at $\approx 266\,\mathrm{cm}^{-1}$ which corresponds to those at the zone edge of the basic Brillouin zone. The splitting of the doublets is 3 to $6\,\mathrm{cm}^{-1}$ and the magnitude of the splitting depends on the experimental configuration of the observation [10]. The splitting at forward scattering geometry is smaller than for back scattering geometry. This dependence arises from the dispersion of the FTA mode. The dependence of ω on wave vector q is large for the FTA mode even at around the Γ point ($q = 0$). The dispersion curves of the FTA modes at around the Γ point were calculated based on a one-dimensional model taking into account the forces up to the third neighbors [9]. The calculated dispersion curves at around $q = 0$ explain well the FTA dispersion obtained from a Raman measurement using laser lines with different wavelengths [10].

For 3C-SiC the TO and LO bands are observed at 796 and $972\,\mathrm{cm}^{-1}$, respectively. The FTO mode corresponding to the zone edge of the basic Brillouin zone is observed at $799\,\mathrm{cm}^{-1}$ in the 2H polytype. In contrast to the FTA and folded longitudinal acoustic (FLA) modes, the splitting of the FTO modes has not been observed, although it is expected from the lattice dynamical calculation. This is because the FTO bands are too broad for the splitting to be observed. As shown in Fig. 2, the folded modes of LA and LO phonon branches are also observed [16, 5], though their intensities are very weak compared with the FTA and FTO modes except for the LO mode with $q = 0$.

A high resolution Raman measurement showed that the band width (FWHM) for the FTA mode at $150\,\mathrm{cm}^{-1}$ in the 6H polytype is less than $0.24\,\mathrm{cm}^{-1}$ at room temperature. On the contrary, the width of the FTO band is large, being about $3\,\mathrm{cm}^{-1}$. The difference of the band widths between the FTA and FTO modes may be due to the difference

in the phonon decay process through the anharmonic potential. It is more likely that there are many decay channels for high frequency FTO modes than for FTA modes.

The FTA, FTO, FLA and FLO modes have been observed for various polytypes [2 to 13]. Since these folded modes correspond to the phonon modes at the reduced wave vector of $x = q/q_B$ in the Brillouin zone of the 3C polytype, the dispersion curves for the transverse and longitudinal phonons in 3C-SiC propagating along the c-direction can be estimated from the frequencies of these folded modes. Fig. 3 shows the derived dispersion curves for 3C-SiC.

The frequency of phonon modes at the Γ point ($q = 0$) has been precisely determined by Raman scattering and infrared absorption (reflection). Table 2 lists the precise frequencies of the folded modes of the transverse and longitudinal phonons obtained from Raman measurements.

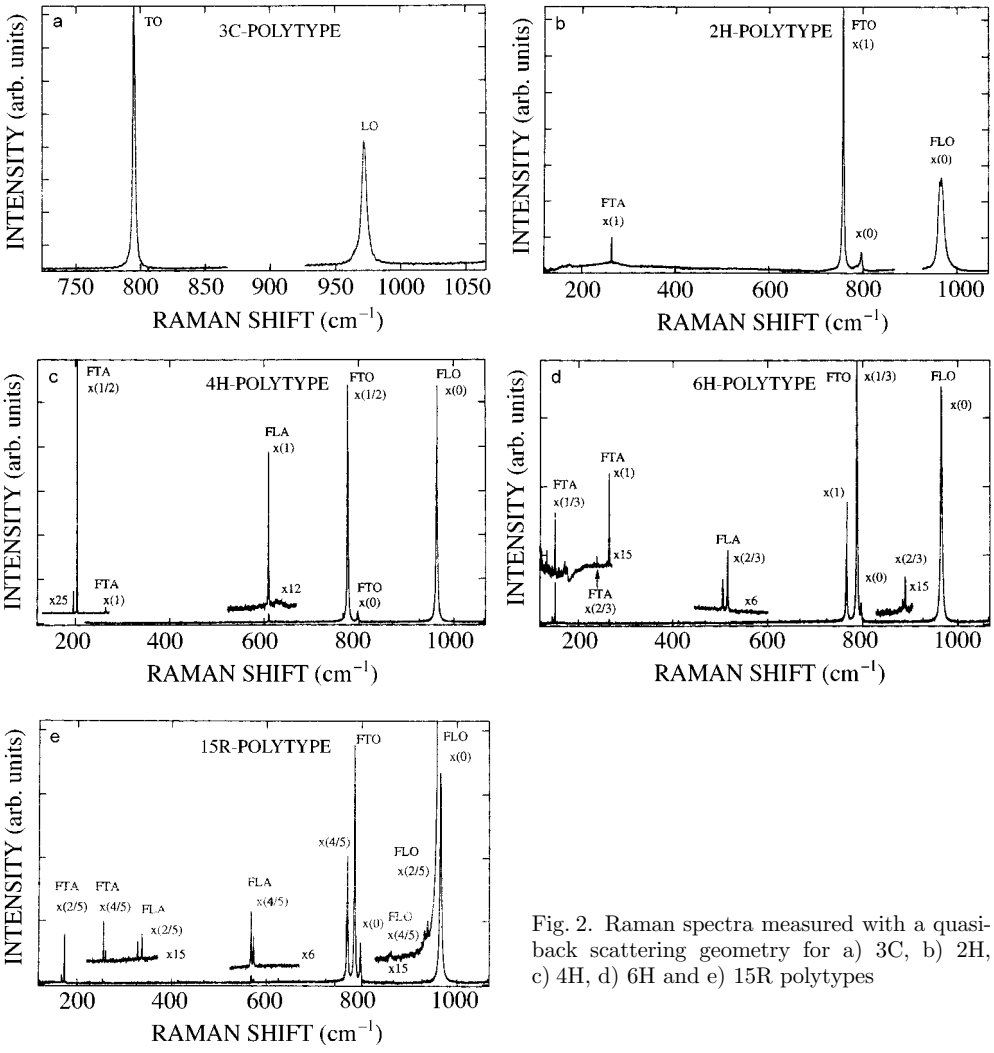

Fig. 2. Raman spectra measured with a quasi-back scattering geometry for a) 3C, b) 2H, c) 4H, d) 6H and e) 15R polytypes

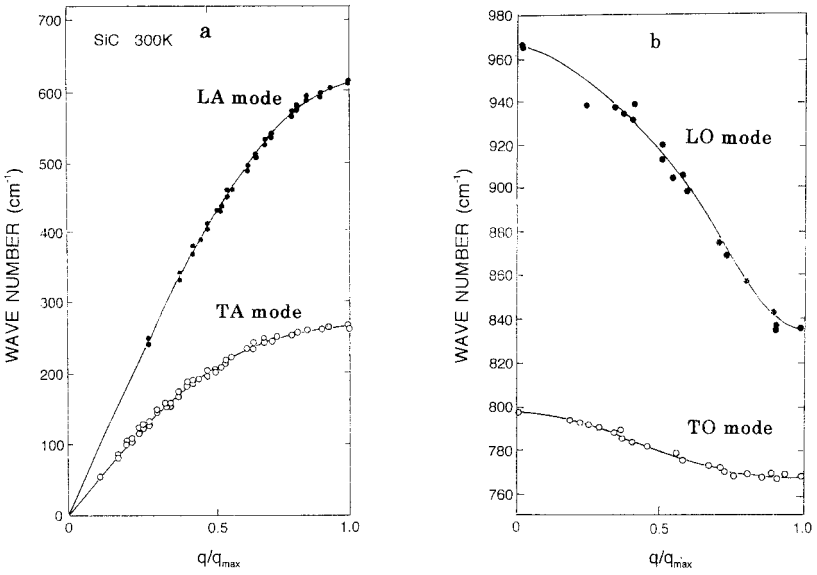

Fig. 3. Phonon dispersion curves of 3C-SiC in the Γ–L direction, which are derived from the frequencies of folded modes in various polytypes [16]. a) Acoustic branch and b) optical branch

Phonons at wave vectors other than the Γ point in the Brillouin zone have been observed by photoluminescence and neutron scattering. The phonon dispersion curves of 3C-SiC have been obtained from neutron scattering. Theoretical calculations of the dispersion curves based on several lattice dynamics models have been made for 3C [17 to 19], 2H [18, 19], 4H [18, 19], and 6H polytypes [19].

4.2 Raman intensity profiles

As shown in Fig. 2, the Raman intensities of the folded modes are not equal even when these modes belong to the same symmetry. The Raman intensity profiles depend strongly on the stacking arrangement of the polytypes. This fact indicates that the intensity profile of the folded modes enables us to identify the stacking arrangement of the polytypes as does the X-ray intensity analysis.

The Raman intensity profiles of the FTA and FTO modes have been calculated for various polytypes based on the bond polarizability model [6, 9, 11, 12]. In this model, the Raman polarizability tensors are obtained as the sum of the contributions from the bond Raman polarizabilities multiplied by the bond length variation. For SiC polytypes, the bond Raman polarizabilities can be approximately expressed by a single parameter for both the FTA and FTO modes. Accordingly, the Raman intensity profile depends only on the atomic displacements in the framework of this model and the calculated Raman intensity profiles are sensitive to the choice of the force constants [9].

The atomic displacement patterns for the planar type modes have been calculated using a one-dimensional model for which we take short-range force constants extended to the third neighbors and taking into account the force difference between cubic and hexagonal environments [9]. In this calculation, the force constants are chosen so that they reproduce not only the experimental phonon frequencies but also Raman intensity

Table 2
Raman frequencies of the folded modes for typical polytypes. Only the FTA and FTO modes with $E(E_1, E_2)$ symmetry and FLA and FLO modes with A_1 symmetry are shown

polytype		frequency (cm^{-1})			
		planar acoustic	planar optic	axial acoustic	axial optic
	$x = q/q_B$	FTA	FTO	FLA	FLO
3C	0	–	796	–	972
2H	0	–	799	–	968
	1	264	764	–	–
4H	0	–	796	–	964
	2/4	196, 204	776	–	–
	4/4	266		610	838
6H	0	–	797	–	965
	2/6	145, 150	789	–	–
	4/6	236, 241		504, 514	889
	6/6	266	767	–	–
8H	0	–	796	–	970
	2/8	112, 117	793	–	–
	4/8	203		403, 411	917, 923
	6/8	248, 252		–	–
	8/8	266	768	615	
15R	0	–	797	–	965
	2/5	167, 173	785	331, 337	932, 938
	4/5	255, 256	769	569, 577	860
21R	0	–	797	–	967
	2/7	126, 131	791	241, 250	
	4/7	217, 220	780	450, 458	905, 908
	6/7	261	767	590, 594	

profiles for various polytypes. The force constant values thus determined are listed in Table 1 of [9].

The Raman intensity for the λ-th mode is given by

$$W_\lambda = A \, \frac{n(\omega)+1}{\omega} \, |\mathbf{e}_i \, \alpha^{(\lambda)}_{\varrho\sigma} \, \mathbf{e}_s|^2 \,, \tag{2}$$

where A is a constant independent of ω, $n(\omega)$ is the Bose factor, and $\mathbf{e}_i(\mathbf{e}_s)$ is the polarization vector of the incident (scattered) light. The Raman tensor component of the λ-th mode with a finite q is given by

$$\alpha^{(\lambda)}_{\varrho\sigma} = d \sum \pm \left[u^{(\lambda)}_{(j)} - u^{(\lambda)}_{(j+1)}\right] \exp\left(iqz_i\right), \tag{3}$$

where d is the xy component of the Raman polarizability tensor. The signs in the above equation depend on the type of the bonds. The plus sign is assigned to the group of the bonds a) α-B, β-C, and γ-A, and the minus sign for the group of the bonds b) α-C, β-A,

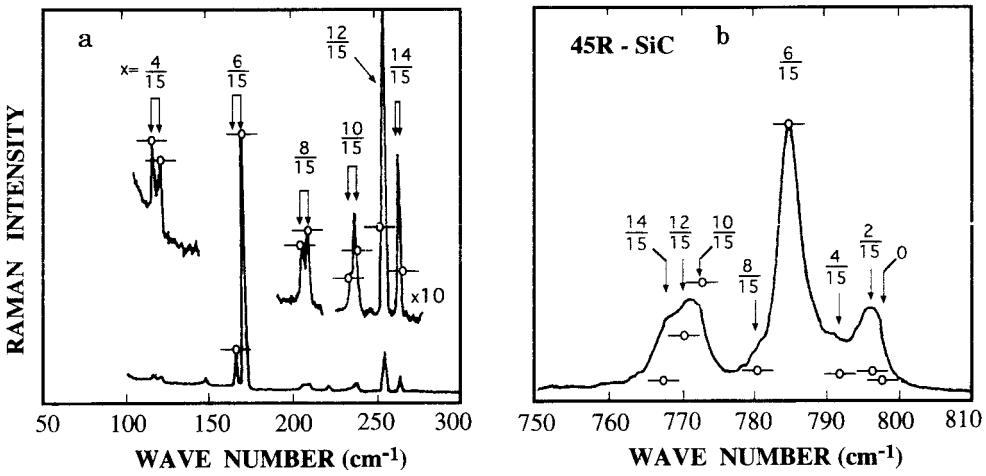

Fig. 4. Comparison of the Raman intensities of observed FTA and FTO modes and calculated ones for the 45R polytype. The calculated intensities are shown by open circles

and γ-B or vice versa. Here, the Latin letters A, B, C and Greek letters α, β, γ represent the positions of silicon and carbon atoms, respectively. $[u_{(j)} - u_{(j+1)}]$ is the relative displacement of the neighboring Si–C atomic planes for which the Si–C bonds are tilted against the c-axis. The displacement amplitudes are obtained by solving the equations of motion. The Raman intensity profiles calculated using Eqs. (2) and (3) reproduce well the observed spectra for various polytypes [9]. In Fig. 4 the calculated and experimental Raman intensity profiles for the 45R polytype are compared as an example. The calculated intensity profile reproduces the observed spectra except for the FTA modes with $x = 12/15$ and 14/15. This discrepancy might arise from the existence of mixtures of other polytypes.

4.3 Anisotropy of the phonon modes

The frequencies of the phonon modes at the Γ point are independent of propagation direction of these phonons in cubic crystals. In uniaxial crystals, anisotropic short-range forces cause the phonon frequency variation with the phonon propagation axis. When electrostatic forces produced by the LO phonon are greater than those due to the anisotropy of the short-range forces as seen in SiC crystals, the LO–TO splitting is greater than the splitting of the axial (A-type) and planar (E-type) mode frequencies. In this case, for a phonon propagating along the direction slant against the c-axis, the frequencies of the LO and TO phonons are given by the following equations [20]:

$$\omega_{\mathrm{LO}}^2 = (\omega_{\mathrm{LO}}^{\mathrm{A}})^2 \cos^2\theta + (\omega_{\mathrm{LO}}^{\mathrm{E}})^2 \sin^2\theta\,, \tag{4}$$

$$\omega_{\mathrm{TO}}^2 = (\omega_{\mathrm{TO}}^{\mathrm{E}})^2 \cos^2\theta + (\omega_{\mathrm{TO}}^{\mathrm{A}})^2 \sin^2\theta\,, \tag{5}$$

where θ is the angle between the c-axis and the phonon propagation vector. This angle dependence of the phonon frequency is called directional dispersion. With back scattering geometry using the c-face, we observe LO modes with A_1 symmetry and TO modes with E (E_2) symmetries. The E_2 mode does not show directional dispersion, because the E_2 mode is infrared inactive and does not accompany the electrostatic field.

Special care is necessary for the characterization of imperfections in α-SiC by the Raman spectroscopy. One should distinguish between the shift of phonon modes due to defects and the anisotropy, because the breakdown of the polarization selection rule due to defects or orientational disorder induces the appearance of otherwise forbidden bands with different frequencies.

4.4 Hexagonality

Some physical quantities in SiC polytypes are scaled by the hexagonality, which is defined as the percentage of the hexagonal stacking in polytypes. The anisotropy of the phonon properties appears remarkably in the E–A splitting of the TO phonon band. The A_1- and E-type TO modes at the Γ point have been measured by Nakashima et al. [8] for various polytypes. The observed frequency splitting of the A_1 (TO) and E (TO) bands is represented empirically as [8]

$$\omega(\mathrm{E_t}) - \omega(\mathrm{A_{1t}}) = 29.4\, h\ (\mathrm{cm^{-1}})\,, \tag{6}$$

where h is the hexagonality. The hexagonality dependence of the LO-phonon frequency is given by Hofmann et al. [19].

When the difference in the forces between the cubic and hexagonal stackings in α-SiC crystals is neglected, the equations of motion for the atoms are reduced to those for cubic SiC. Under this assumption we obtain a simple expression for the Raman scattering efficiency as

$$I(\omega) = A[n(\omega)+1]\,\omega^{-1}\,|u(\omega)-v(\omega)|^2\,|\textstyle\sum c(m)\,\exp(-iqz_m)|^2\,, \tag{7}$$

where $n(\omega)$ is the Bose factor, u and v are displacement amplitudes of Si and C planes in a unit cell, and q is the wave vector of the phonon. Here

$$c(m) = \textstyle\sum \alpha'(n)\,\alpha'(n+m) \tag{8}$$

is the autocorrelation function of the bond Raman polarizability and α' is the bond Raman polarizability between the Si and C planes. The arrangement of the bond Raman polarizability in the unit cell of the polytypes is easily written down if the polytype structure is given. For example, that of the 6H polytype is given by

$$\alpha'/d = (1,1,1,-1,-1,-1)\,, \tag{9}$$

where d is the tensor component of the bond Raman polarizability. The calculation of the Raman intensity profiles using Eqs. (7) and (8) reveals that the Raman intensity for a polytype has a maximum for the FTA and FTO modes having a reduced wave vector of $q/q_\mathrm{B} = h$, where h is the hexagonality.

As shown in Fig. 2, the intensity of the FTA and FTO modes at $q/q_\mathrm{B} = 0.33$ shows a maximum for the 6H polytype. This simple relationship between the hexagonality of the polytype structure and the reduced wave vector of the folded mode having maximum intensity has been confirmed experimentally [12] for higher polytypes up to 66R as shown in Table 3.

As mentioned before, the intensities of the FLA and FLO modes except the mode with $q = 0$ are much weaker than those of the FTA and FTO modes. The weak intensity may result from the cancellation of the contributions from the bond Raman polarizabilities for these modes.

Table 3
The hexagonality and the reduced wave vector of the folded modes which show the strongest intensity for each branch [12]

polytype	$x = q/q_B$ for I_{max} mode	hexagonality
4H: 22	$2/4 = 0.5$	0.5
15R: $(32)_3$	$2/5 = 0.4$	0.4
6H: 33	$2/6 = 0.33$	0.33
21R: $(34)_3$	$2/7 = 0.28$	0.28
8H: 44	$2/8 = 0.25$	0.25
27R: $(22\ 23)_3$	$4/9 = 0.44$	0.44
33R: $(33\ 32)_3$	$4/11 = 0.36$	0.36
45R: $[(32)_2 23]_3$	$6/15 = 0.4$	0.4
51R$_1$: $[(33)_2 32]_3$	$6/17 = 0.353$	0.353
51R$_3$: $(43\ 32\ 23)_3$	$6/17 = 0.353$	0.353
66R: $[(33)_2(32)_2]_3$	$8/22 = 0.364$	0.364

4.5 Second-order Raman spectra

The scond-order Raman scattering spectra have rarely been studied, although the first-order spectra are well understood. Recently, the second-order Raman spectra of 3C-SiC have been measured and compared with calculated spectra by Windl et al. [21]. A good agreement is obtained between experimental and theoretical Raman intensity profiles. Attempts to use the second-order Raman spectra for the characterization of SiC crystals have not been made so far.

5. Characterization of SiC Crystals

5.1 Polytype identification

Polytypes with longer periods can be identified by the following procedure;

(i) The period is estimated from the FTA and FTO frequencies.

(ii) Possible model structures are listed up and the observed spectrum is compared with those calculated for these model structures [8, 13]. The best-fit structure gives us the polytype structure. Up to now the longest polytype determined from the Raman intensity analysis is 132R polytype: $[(33)_3(32)_2(33)_2 22]_3$ in Zhdanov notation [13].

The identification of the common polytypes with shorter period is easy. The necessary things to do are to obtain the precise frequency values of the FTA and FTO modes in order to determine the period and to seek a folded mode which has maximum intensity. As mentioned in Section 4.4, there is a simnple rule that the reduced wave vector of the folded mode with a maximum intensity, $x = q/q_{max}$ is equal to the hexagonality of the polytype [12]. From these measurements one can quickly identify the short period polytypes. When using a Raman microscope, the stacking structure in local areas of μm size is inferred.

The FTA bands are useful to determine the period, because these bands are very narrow. For the sharp band shape, the FTA modes can be used to identify the polytype structure, evaluate strains and also study stacking disorders.

5.2 Stacking disorder of SiC

The Raman bands in SiC crystals containing stacking disorders exhibit broadening and distortion. This feature is clearly observed for the FTA modes. For heavily disordered

crystals one finds a broad background which partly reflects the phonon density of states as shown in Fig. 5 [22]. An interesting thing is that the peak of the broad band lies around the frequency of the FTA modes at $x = 0.33$ in the 6H polytype. This implies that this disordered crystal contains many short-range 6H (33 in Zhdanov notation) stacking structures. Similar spectral profiles are often observed for disordered SiC samples grown by the Acheson method: one finds broad and distorted Raman bands corresponding to the FTA modes in common polytypes (6H, 15R and 4H).

The spatial distribution of the stacking faults is usually not uniform. The results of X-ray diffraction and synchrotron edge topography showed that disordered layers in SiC crystals are often sandwiched between the same or different polytype regions or exist near the surface regions [16]. The thickness of the disordered layer is considered to range from about 0.1 to 100 μm. The distribution of the disordered layer has been measured by use of a Raman microscope. An example of Raman image measurements is shown in Fig. 6. A disordered region with a thickness of about 20 μm is observed between the 6H and 15R polytype regions.

The characteristic feature of disordered SiC is the remaining of short-range ordering: the disorder is not completely random and the disordered structure consists of a combination of randomly disordered simple polytype domains such as 6H, 15R, 4H, etc. and those in which stacking faults are distributed periodically or nearly periodically.

The Raman spectral profiles of the disordered crystals have been calculated for various model structures consisting of random domains based on "33" and "32" stackings

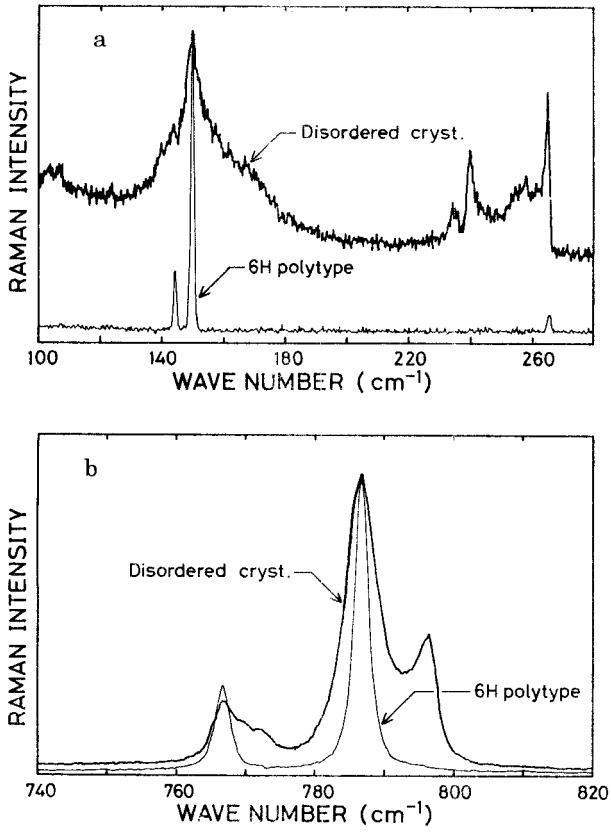

Fig. 5. Raman spectra of a heavily disordered SiC crystal for a) FTA and b) FTO modes

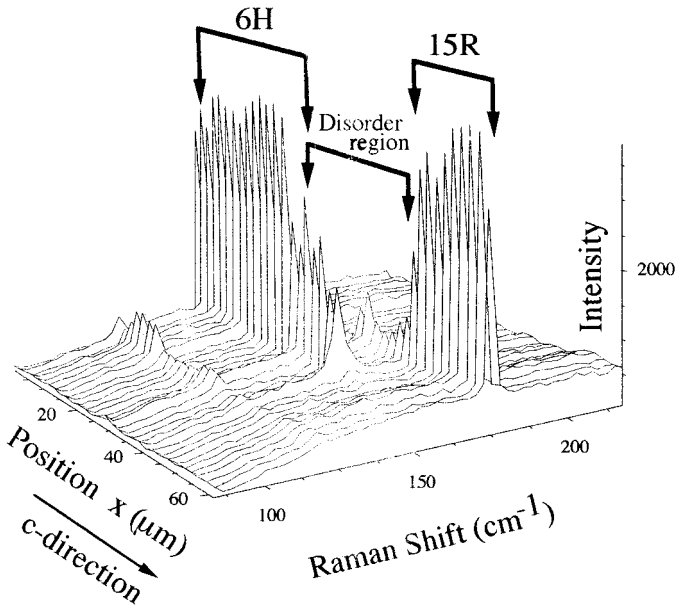

Fig. 6. One-dimensional Raman image of the disordered SiC. Their disordered region sandwiched between the 6H and 15R regions consists mainly of a mixture of "33" and "32" stacking domains

and stacking faults, and compared with observed spectra [22]. The results of the simulation demonstrate that the Raman spectral profile is quite useful to evaluate (i) the degree of the disorder, (ii) average domain size and (iii) dispersion of the domain sizes, although a quantitative evaluation of the disordered stacking structure is difficult.

5.3 Evaluation of stress

Phonon Raman bands in crystals shift with stress, because the atomic distances, in other words, the bonding forces are changed by the stress. The behavior of the Raman bands in 3C-SiC under hydrostatic pressure has been studied by Olego et al. [23]. The frequencies of the TO and LO modes against the relative lattice compression are given (in units of cm^{-1}) by

$$\omega(\mathrm{TO}) = 796.5 + 3734(-\Delta a/a_0)\,, \tag{10}$$

$$\omega(\mathrm{LO}) = 973 + 4532(-\Delta a/a_0)\,, \tag{11}$$

where a_0 is the lattice constant.

The mode Grüneisen parameters obtained for the TO and LO bands are 1.55 and 1.56, respectively, being larger than the values for silicon and diamond [23]. Olego et al. found a slight increase of the LO–TO splitting with pressure and suggested that the transverse effective charge varies with pressure.

Raman spectra of 6H-SiC under ultrahigh pressures up to 95 GPa has been measured by Liu and Vohra [24]. The mode-Grüneisen parameters they obtained is $\gamma = 1.23$ for TO and LO modes. They observed that the LO–TO splitting increases with increasing pressure and saturates above 60 GPa. The transverse effective charge estimated from the splitting shows a decrease at high pressures, indicating the increase of covalent bonding at the high pressures.

The study of the phonon modes under uniaxial or two-dimensional stress is an important subject for SiC. The two-dimensional stress is often found in hetero-epitaxial films. The effect of the stress on Raman bands for 3C-SiC films grown on Si crystals has been measured by Mukaida et al. [25] and Feng et al. [26].

Mukaida et al. compared the frequencies of the LO phonon band of as-grown films and films annealed after removing the substrate. They observed a down-shift of the LO band by about 2 cm^{-1} as compared with the annealed films. The stress estimated assuming that the annealed films are stress-free is 5.4×10^8 Pa. This value is too small for the epitaxial films completely lattice matched with the substrate, indicating that the stress is partially relaxed in their SiC/Si specimens. They also showed that the stress in the 3C-SiC films on Si(111) is a little larger than that on Si(100). The TO mode is expected to be forbidden in a back scattering geometry, if the epitaxial films are perfect single crystals and (100) oriented. However, TO modes were observed for 3C-SiC films annealed at 1750 °C after removal of the substrate, although the as-grown films grown on Si(100) did not show the TO mode. This fact was attributed to the occurrence of stackings faults in the annealed films. A similar result was obtained by Feng et al. [26]. They confirmed that 3C-SiC grown on Si(100) has the same orientation as that of the substrate. The strain in SiC films estimated from the Raman measurement was 0.1 to 0.2%. They also observed the forbidden TO band and enhancement of the LO band in 3C-SiC films with the substrate removed. This fact was attributed to the multireflection of the incident light in the films, which made the forward and back scattering observable.

More recently, DiGregorio et al. measured the TO-mode peakshift in 3C-SiC whiskers to evaluate residual stresses in an Al_2O_3/3C-SiC composite under hydrostatic pressure in a diamond anvil cell [27]. In another experiment with a microtension apparatus for an individual whisker they also obtained a Raman-stress coefficient for uniaxial stress along [111].

5.4 Polytype conversion

The thermal treatment at high temperatures induces polytype conversion. The transformation of the β-type into α-type SiC has been studied by Raman scattering [28, 29]. For 3C polytypes annealed above 2000 °C, the conversion from 3C into the 6H or 15R polytype has been observed. The polytype conversion at early stages of the annealing is not uniform. The spatial distribution of the converted polytype regions is easily measured by a Raman microprobe technique.

5.5 Damages by ion implantation

Ion implantation gives damages to crystals and the increase of the ion dose transforms the crystals to an amorphous state eventually. The damages in solids introduced by the ion implantation have been characterized by Raman spectroscopy [15]. Raman spectra of ion implanted SiC have been observed in several institutes. The first order Raman bands decrease in intensity with increasing ion dose and broad disorder-activated bands appear.

Fig. 7 shows a Raman spectrum of 6H-SiC implanted with N^+ ions at multidifferent energies which are measured with a confocal Raman microscope. The fluence is 5×10^{14} cm^{-2} and the thickness of the damaged layer is about 0.4 μm. Broad Raman bands are observed below 1000 cm^{-1} superimposed on sharp Raman lines, which arise from the underlying crystal. The spectral profile of the broad bands resembles the calcu-

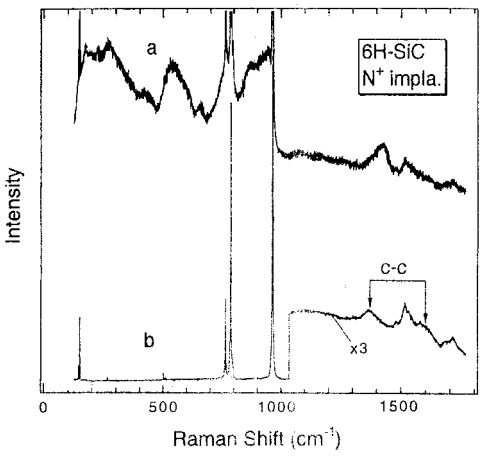

Fig. 7. Raman spectra of an (a) ion implanted and (b) subsequently annealed 6H-SiC crystal

lated phonon density of state [19] qualitatively. On annealing the implanted samples at elevated temperatures, the Raman bands grow again following recovery of the crystallinity. However, weak bands still remain at around 1370 and 1600 cm^{-1}, which may be due to defective C–C networks in the implanted region.

The damaged layers induced by the ion implantation are usually limited in the surface region, the excitation laser light for which SiC is transparent probes the damaged layer and also undamaged substrates simultaneously. In order to evaluate the damaged layer quantitatively, one must use ultraviolet laser light which is absorbed in the near surface region or a confocal microscope system and probe only the damaged layer.

6. Raman Characterization of Electronic Properties in SiC

A wide variety of electronic excitations in semiconductors can be studied by the Raman scattering technique [30, 31]. A pioneering work on the electronic Raman scattering in silicon carbides was reported more than two decades ago by Colwell and Klein [32]. They observed excitations of bound electrons, plasma oscillations coupled with LO phonons and a Fano interference between the phonon and electronic excitations. In the past, electronic excitation in SiC was studied much less actively than in more common semiconductors like Si and GaAs, due primarily to the lack of high quality crystals. Quite recently, however, good single crystals with high homogeneity and well-controlled doping of impurities suitable for electronic device applications have become available for some common SiC polytypes, and electronic Raman scattering experiments on silicon carbides have been revived.

In the following, some basic aspects of the electronic Raman scattering in SiC crystals are surveyed using recent Raman spectral data.

6.1 Raman scattering from bound electrons

Silicon carbides have multiple equivalent conduction band minima located at non-zero wave vectors. For example, 3C has three equivalent minima at the X point in the f.c.c. Brillouin zone, while 4H (6H) has three (six) equivalent minima located at M(ML) point in the hexagonal Brillouin zone [33, 34]. Consequently the donor ground state is degen-

erate. In SiC, the central cell potential caused by the impurity atom has the C_{3v} site symmetry and splits the gorund state into the 1s(A) and 1s(E) levels [32]. The transition between the 1s(A) and 1s(E) levels is called the valley–orbit transition, which has been previously observed in 4H, 6H and 15R polytypes [32].

Fig. 8 shows typical Raman spectra of nitrogen-doped n-type 6H-SiC with different carrier densities, which are taken at 300 K and 35 K. As marked by the arrows, three sharp bands appear in the more lightly doped sample at low temperature (Fig. 8a), and the band at the lowest energy (105 cm^{-1}) totally disappears at room temperature [35]. Since these three transitions have E_2 symmetry as confirmed by polarization measurements, and since their appearance is similar to three zero-phonon lines observed in emission spectra [36], Colwell and Klein [32] assigned these bands to 1s(A) → 1s(E) valley–orbit transitions of electrons bound to donor impurities at three inequivalent sites; the 105 cm^{-1} band corresponds to a hexagonal (h) site, and the higher-energy bands at 486 and 505 cm^{-1} to two cubic (c) sites. In the more heavily doped sample (Fig. 8b), the 105 cm^{-1} band disappears and the higher frequency ones broaden even at low temperatures.

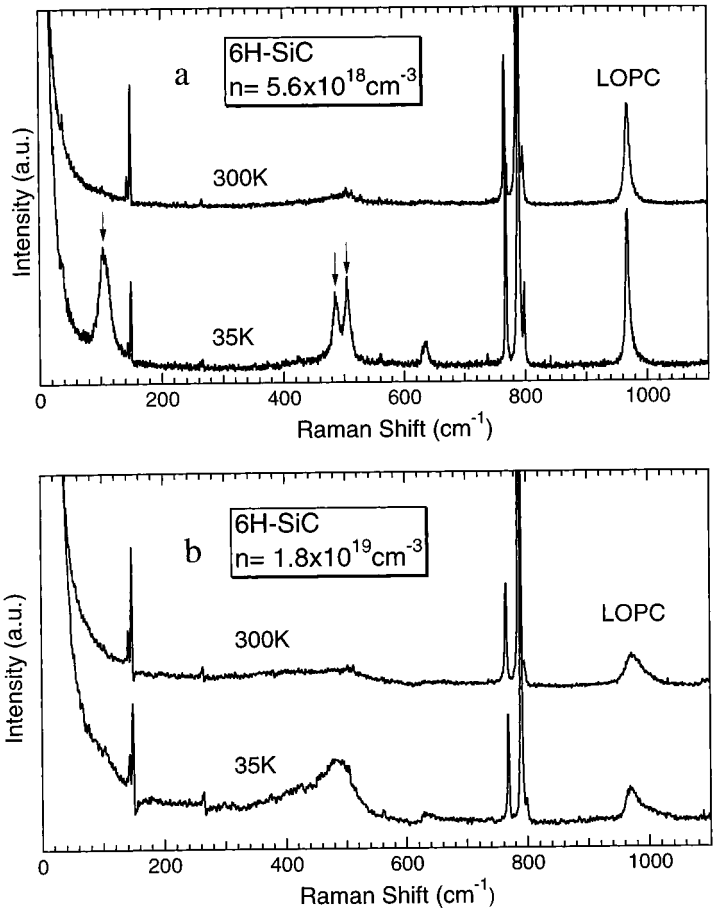

Fig. 8. Raman spectra of 6H-SiC at different temperatures and carrier densities [35]

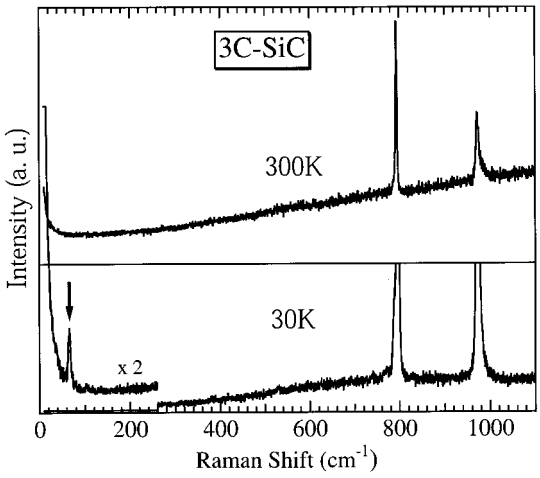

Fig. 9. Raman spectra of 3C-SiC at different temperatures (a.u. means arbitrary units)

3C-SiC has, on the contrary, only a c-site. Therefore, no such multiplicity of the valley–orbit transition is expected. Actually, as seen in Fig. 9 we can observe only a sharp band at 66 cm^{-1} at low temperatures. A similar band was previously reported by Vakulenko et al. [37]. This transition shows E-type symmetry, which is consistent with the assignment of 1s(A) $\rightarrow$ 1s(E) transition. Furthermore, this assignment is strongly supported by a recent infrared absorption experiment [38], where two distinct series of donor transitions, 1s(A) $\rightarrow$ np and 1s(E) $\rightarrow$ np for $n = 2$ to 6, are clearly observed in a high-resolution spectrum. According to the donor level scheme deduced from the absorption experiment the 1s(A) – 1s(E) splitting is given by 67 cm^{-1}, which is in excellent agreement with the Raman result.

To our knowledge, the correspondence of multiplicity between the inequivalent donor sites and the number of valley–orbit transitions observed has not been well understood in other polytypes. Fig. 10 shows typical Raman spectra for 4H-SiC with different carrier densities. Although two inequivalent sites are expected (one c-site and one h-site), only a sharp band appears at 57 cm^{-1} and very weak and broad ones are observed at about 530 and 570 cm^{-1} in the more lightly doped sample (Fig. 10a). The sharp peak smears out in the more heavily doped sample (Fig. 10b) [39]. Fig. 11 shows the result of 15R-SiC. Contrary to the five inequivalent sites expected (three c-sites and two h-sites), only three sharp peaks appear clearly below 100 cm^{-1}, in addition to weak and complex bands around 400 cm^{-1}. Electronic Raman scattering was also reported in 6H-, 15R-, and 27R-SiC by Gorban et al. [40] and in 21R-SiC by Azhnyuk et al. [41]. Their results are summarized together with other data in Table 4, where the number of Raman peaks observed at low temperatures and that of inequivalent donor sites are compared. For 4H, 15R, 21R and 27R, there are some ambiguities in the number of high-energy bands (350 to 700 cm^{-1}), because most of the bands are very weak and not well separated. This table shows that there is not a clear correspondence between the number of inequivalent sites and the observed Raman peaks. Gorban et al. raised a question whether the electronic Raman spectra can be interpreted simply from the standpoint of h- and c-type inequivalent sites [40]. It is also not yet clear how the site character (h- or c-type) is related to the energy of the electronic transitions, and why the higher-energy electronic

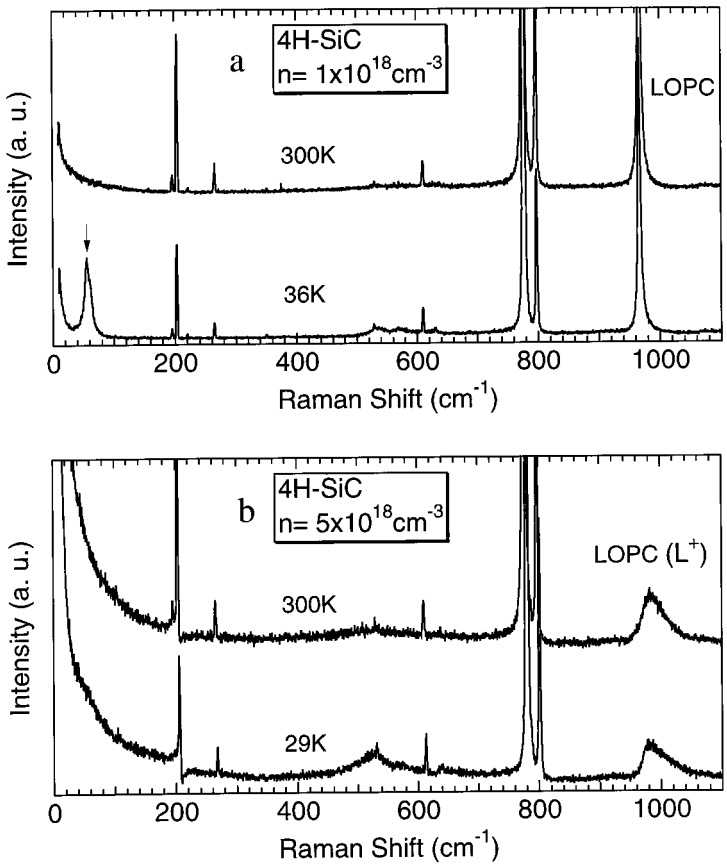

Fig. 10. Raman spectra of 4H-SiC at different temperatures and carrier densities [39]

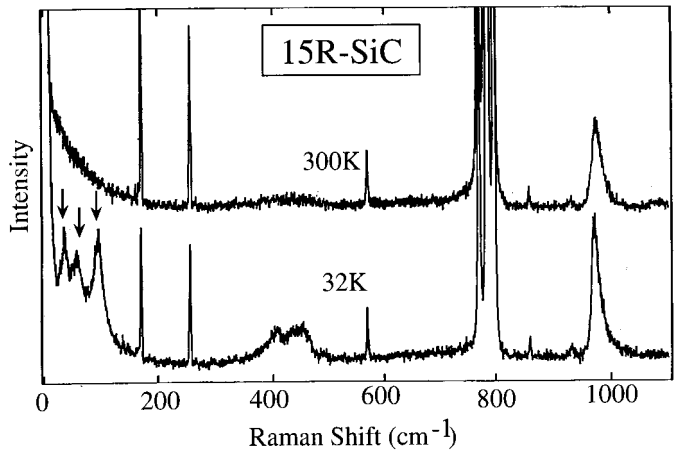

Fig. 11. Raman spectra of 15R-SiC at different temperatures

Table 4
Number of inequivalent donor sites and electronic band peaks observed at low temperature

polytype	inequivalent sites		observed peaks		ref.
	h-site	c-site	low-freq.	high-freq.*)	
3C	–	1	1	–	[37]
6H	1	2	1	2	[32]
4H	1	1	1	–**)	[35]
15R	2	3	3	2 to 3	[32, 40]
21R	2	5	2	4 to 6	[41]
27R	2	7	3	3	[40]

*) Electronic bands often appear in groups well separated in frequency. Here, the bands appearing at less than about 200 cm^{-1} are classified as low-frequency modes, while those at 350 to 700 cm^{-1} are classified as high-frequency modes.
**) Weak structures at 500 to 650 cm^{-1} are not included.

bands are weak and broad except for the 6H polytype. More detailed experimental work using high quality crystals is obviously needed together with theoretical reconsideration on the classification by inequivalent impurity sites.

6.2 Raman scattering from free carriers

6.2.1 LO phonon–plasmon coupled modes

In a polar semiconductor collective excitation of free carriers (plasmon) interacts with the longitudinal optical (LO) phonon via their macroscopic electric fields, to form the LO phonon–plasmon coupled (LOPC) mode. The Raman lineshape of the LOPC mode changes sensitively with the free carrier density (n). A comparison of the LOPC profiles for different n values is shown in Fig. 8 for 6H-SiC and in Fig. 10 for 4H-SiC. The LOPC bands are broad and their peaks are shifted to higher frequency with increasing n. The carrier density dependence of LOPC profiles has also been studied in n-type 3C-SiC [42].

Since 6H- and 4H-SiC are uniaxial crystals, LOPC has anisotropy between the mode with the atomic displacement parallel to the c-axis (axial mode) and that with the atomic displacement perpendicular to the c-axis (planar mode) [43]. Fig. 12 shows details of the LOPC profiles for the axial and planar modes of 6H-SiC, and in Fig. 13 their peak intensity, FWHM(full width at half maximum) and peak shift are plotted against n. The planar mode shows larger variation than the axial mode in all these quantities, suggesting that 6H-SiC has a large anisotropy. On the contrary, 4H-SiC shows smaller anisotropy [43].

The dashed lines in Fig. 12 are the best fits to the observed profiles. We can deduced carrier transport parameters from the lineshape fitting analysis as described below.

6.2.1.1 Lineshape analysis

The LOPC mode has two branches (L^+ and L^-), and their energies are given by the zeros of the real part of the total dielectric function. Three mechanisms generally contri-

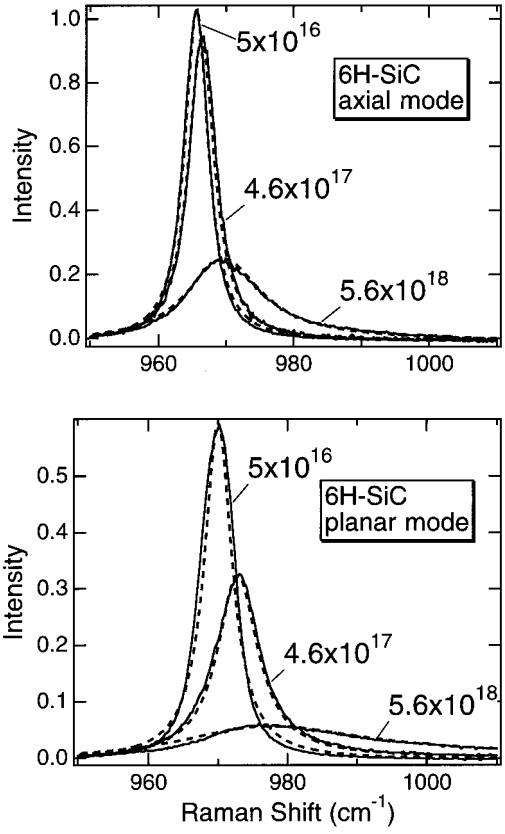

Fig. 12. LOPC profiles for 6H-SiC for different carrier densities. Dashed lines denote best-fit calculations [43]

bute to the Raman scattering by the LOPC mode; deformation potential (DP) and electro-optical (EO) mechanisms and charge-density fluctuation (CDF) [44]. In semiconductors such as SiC which have large band gap and low carrier mobility, the EO and DP mechanisms dominate the scattering process and the lower-energy branch (L^-) is not observed in the Raman spectra because of the strong damping (overdamping). In this case, only the L^+ mode is clearly observed as demonstrated in Figs. 8 and 10.

Here, we briefly outline a theoretical treatment of the LOPC lineshape for cubic crystals, and then extend it to the hexagonal systems. The Raman band profile of the coupled mode for cubic crystals is written as [45]

$$I(\omega) = SA(\omega)\,\mathrm{Im}\,\{-1/\varepsilon(\omega)\}\,, \tag{12}$$

where ω is the Raman shift, S is a proportionality constant, $\varepsilon(\omega)$ is the dielectric function, and $A(\omega)$ is given by

$$\begin{aligned} A(\omega) = 1 + 2C\omega_{\mathrm{T}}^2[\omega_{\mathrm{p}}^2\gamma(\omega_{\mathrm{T}}^2-\omega^2) - \omega^2\Gamma(\omega^2+\gamma^2-\omega_{\mathrm{p}}^2)]/\Delta + C^2(\omega_{\mathrm{T}}^4/\Delta) \\ \times [\omega_{\mathrm{p}}^2\{\gamma(\omega_{\mathrm{L}}^2-\omega_{\mathrm{T}}^2) + \Gamma(\omega_{\mathrm{p}}^2-2\omega^2)\} + \omega^2\Gamma(\omega^2+\gamma^2)]/(\omega_{\mathrm{L}}^2-\omega_{\mathrm{T}}^2)\,. \end{aligned} \tag{13}$$

Here, ω_{T} and ω_{L} are the TO and LO phonon frequencies, respectively, γ is the plasma damping constant, Γ is the phonon damping constant, and

$$\Delta \equiv \omega_{\mathrm{p}}^2\gamma[(\omega_{\mathrm{T}}^2-\omega^2)^2 + (\omega\Gamma)^2] + \omega^2\Gamma(\omega_{\mathrm{L}}^2-\omega_{\mathrm{T}}^2)\,(\omega^2+\gamma^2)\,. \tag{14}$$

C is the so-called Faust-Henry coefficient [46]. The dielectric function $\varepsilon(\omega)$ is given by the contributions from phonon and plasmon,

$$\varepsilon(\omega) = \varepsilon_\infty\left[1 + \frac{\omega_{\mathrm{L}}^2-\omega_{\mathrm{T}}^2}{\omega_{\mathrm{T}}^2-\omega^2-i\omega\Gamma} - \frac{\omega_{\mathrm{p}}^2}{\omega(\omega+i\gamma)}\right]. \tag{15}$$

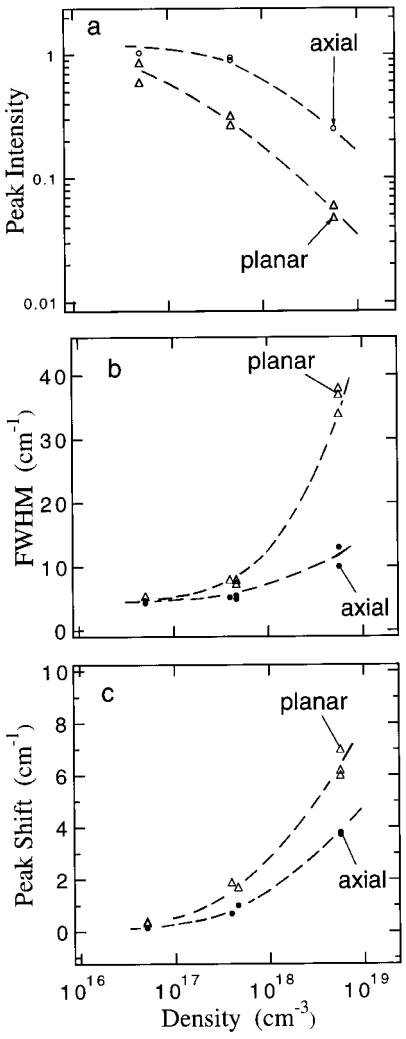

Fig. 13. Peak intensity, FWHM, and peak shift of LOPC in 6H-SiC against carrier density. The peak shift is measured from the peak positions for the undoped samples; 964.5 cm^{-1} (axial mode) and 969.8 cm^{-1} (planar mode) [43]

The plasmon frequency ω_p is given by

$$\omega_p = \sqrt{\frac{4\pi n e^2}{\varepsilon_\infty m}}, \tag{16}$$

where ε_∞ is the optical dielectric constant, n is the carrier density and m is the electron effective mass.

Next, we extend the above treatment to the uniaxial α-SiC crystals. In principle, the effective mass tensors in the hexagonal systems can be described by three independent components of m_{xx} and m_{yy} which are the (transverse) components along MΓ and MK in the Brillouin zone, and m_{zz} which is the (longitudinal) component along ML or the c-axis. However, since the x- and y-directions are not distinguished in the present study, we assume only two independent components, $1/m_\parallel \equiv (1/m)_{zz}$ and $1/m_\perp \equiv (1/m)_{xx} = (1/m)_{yy}$. Therefore, the effective mass $m_\perp$ deduced in this study should be considered as an average of the two transverse components m_{xx} and m_{yy},

$$m_\perp = \sqrt{m_{xx} m_{yy}}\,. \tag{17}$$

This means that the constant energy surface at the conduction band minima is given by a spheroid with the principal z-axis along the c-axis. In this case, the above equations (12) to (17) can be applied to the axial and planar modes independently by defining the following different sets of parameters for the axial (∥) and planar (⊥) modes, respectively; uncoupled TO and LO frequency $\omega_T^{\parallel,\perp}$ and $\omega_L^{\parallel,\perp}$, plasma frequency $\omega_p^{\parallel,\perp}$, damping rate of phonon and plasmon $\Gamma_{\parallel,\perp}$ and $\gamma_{\parallel,\perp}$, Faust-Henry coefficient $C_{\parallel,\perp}$ and optical dielectric constant $\varepsilon_\infty^{\parallel,\perp}$. The proportionality constant S takes different values for each mode. We have fitted Eq. (12) to the observed planar and axial mode profiles individually using $\omega_p^{\parallel,\perp}$, $\gamma_{\parallel,\perp}$ and $\Gamma_{\parallel,\perp}$ as adjustable parameters. Particular attention has been paid in the fitting to reproducing (i) the peak intensity with treating S as a proportionality constant, which is independent of the carrier density, (ii) the peak shift from the uncoupled LO phonon frequency, and (iii) the asymmetric band shape. The fitting of the peak intensity is quite important for the unique determination of the parameters.

6.2.1.2 Carrier transport properties

The free carrier density can be deduced from the plasmon frequency $\omega_{\mathrm{p}}^{\parallel,\perp}$ using Eq. (16), if the effective masses $m_{\parallel}$ and $m_{\perp}$ are known. Since the experimental values reported so far scatter, we have determined the effective masses so that the carrier densities deduced from the Raman study coincide with those from the Hall measurements. In 6H-SiC, by assuming highly anisotropic masses ($m_{\parallel} = 1.4m_0$ and $m_{\perp} = 0.35m_0$), we have obtained a fairly good agreement in carrier density betweeen the Raman experiment and Hall measurements as shown in Fig. 14. Such a large anisotropy of effective mass, $m_{\parallel}/m_{\perp} \approx 4$, is in agreement with recent experimental and theoretical work. On the contrary, a smaller anisotropy has been obtained for 4H-SiC; $m_{\parallel} = 0.48m_0$ and $m_{\perp} = 0.30m_0$ [43].

The carrier mobilities can also be evaluated using the effective masses $m_{\parallel,\perp}$ and plasma damping rates $\gamma_{\parallel,\perp}$ by $\mu_{\parallel,\perp} = e/(m_{\parallel,\perp}\gamma_{\parallel,\perp})$. In Fig. 15a the mobilities of 4H-SiC are plotted against the carrier density n, comparing with the data of a Hall measurement by Götz et al. [47]. Here, all the samples were grown by the modified Lely method. Our results is in quantitative agreement with their values within ±30%. Fig. 15b shows the result of 6H-SiC with recent Hall mobility data for CVD homo-epitaxial layers, and bulk samples prepared by modified-Lely and LPE methods for comparison [48, 49]. The mobilities of our samples prepared by the modified-Lely method are 2 to 5 times smaller than those of the CVD films at large n. This difference is probably attributed to superior crystalline quality of the CVD samples.

The deduced mobilities are also anisotropic: In 4H-SiC, the perpendicular component is slightly larger than the parallel component, $\mu_{\perp}/\mu_{\parallel} \approx 1.2$. This is contrast with 6H-SiC, where large anisotropy has been clearly observerd; $\mu_{\perp}/\mu_{\parallel} \approx 2.0$.

6.2.2 Semiconductor-to-metal transition

Low resistivity SiC crystals are important as electrically conductive substrates for high-power/high-frequency electronic devices with good ohmic contacts. However, basic electronic properties of heavily doped SiC are not yet well known. For example, it is not clear, unlike Si and Ge, at which carrier density SiC undergoes a semiconductor-to-metal

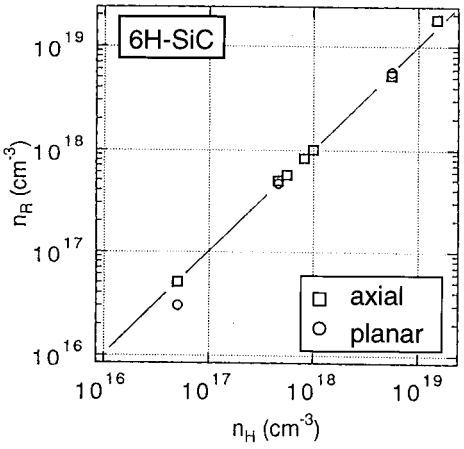

Fig. 14. Comparison of carrier densities deduced from Hall measurements (n_{H}) and Raman experiments (n_{R})

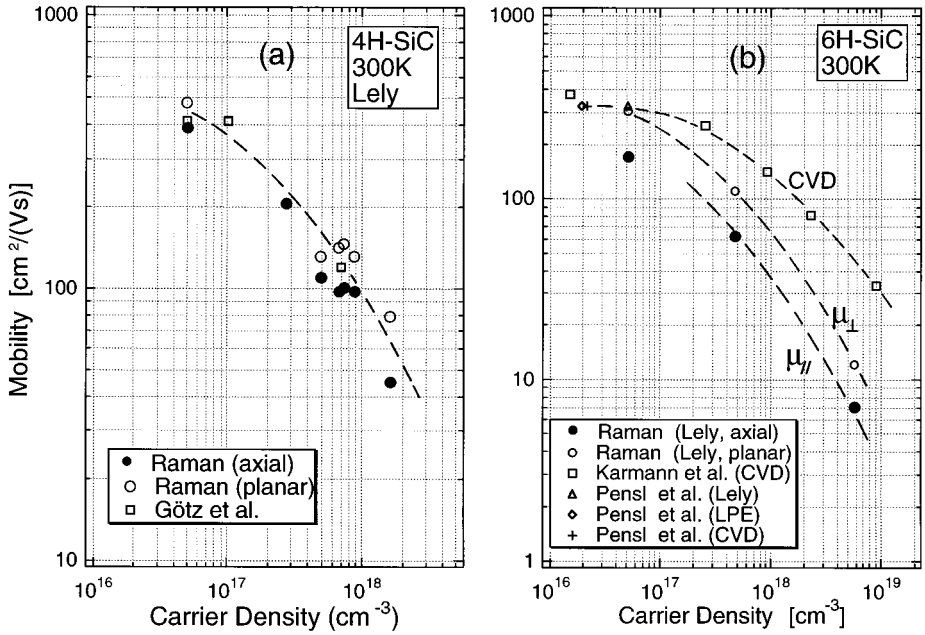

Fig. 15. Mobilities deduced from Raman scattering (open and filled circles) for a) 4H-SiC and b) 6H-SiC [43]. Hall mobility data by Götz et al. [47], Karmann et al. [48] and Pensl and Choyke [49] are also plotted for comparison. The dashed lines are drawn to guide the eyes

transition. We will show that the electronic Raman measurement enables us to distinguish between semiconducting and metallic (degenerate semiconducting) regimes.

As shown in Fig. 8a, a 6H-SiC crystal with $n \approx 6 \times 10^{18}\,\mathrm{cm}^{-3}$ exhibits sharp 1s(A)–1s(E) valley–orbit transitions at 35 K. This fact implies that the donor electrons at the ground state are well isolated from neighboring ones, and the free carriers freeze out efficiently as the temperature is lowered. The carrier freezing is also apparent from the change of the LOPC lineshape because its width decreases remarkably at low temperatures. A detailed analysis of LOPC shows that n decreases from 6×10^{18} to $2 \times 10^{18}\,\mathrm{cm}^{-3}$ as the temperature is lowered from 300 to 35 K. On the contrary, in a more heavily doped sample shown in Fig. 8b with $n \approx 1.8 \times 10^{19}\,\mathrm{cm}^{-3}$ at 300 K, the LOPC band is much broader and highly asymmetric irrespective of the temperature. This means that the carrier freezing is much less efficient. Actually, our LOPC lineshape analysis shows that the free carrier density decreases only to $1.6 \times 10^{19}\,\mathrm{cm}^{-3}$ when the temperature is lowered down to 35 K. Combining with the fact that the sample has a very low resistivity ($5 \times 10^{-3}\,\Omega\,\mathrm{cm}$ at 300 K), our result indicates that a metallic transition occurs around $\approx 2 \times 10^{19}\,\mathrm{cm}^{-3}$. This conclusion is consistent with the fact that the valley–orbit transition band at $105\,\mathrm{cm}^{-1}$ smears out in this sample: Above this critical density a large fraction of electrons may not be bound to individual donors even at low temperatures. Previously, from the temperature dependence of Hall coefficient and resistivity, a critical carrier density of $n_c \approx 2 \times 10^{19}\,\mathrm{cm}^{-3}$ has been suggested for 6H-SiC [50]. The present Raman experiment agrees with this result.

It should be noted that, contrary to the valley–orbit transition at 105 cm^{-1}, the other electronic bands at ≈500 cm^{-1} are still clearly observed at 35 K although they are broadened to merge. It indicates that the electrons at this impurity site (c-site) [32] still retain the character of localization to some extent.

In the case of 4H-SiC, $n_c \approx 5 \times 10^{18}$ cm^{-3} was estimated from the measurement of the LOPC modes and the valley–orbit transitions as seen in Fig. 10b. The fact that 4H has smaller critical density than 6H can be roughly understood by the difference of donor binding energy, or equivalently the Bohr radius a_H, using the well-known Mott criterion $n_c \approx (0.25/a_H)^3$. We have evaluated a_H by the effective mass approximation, although it is not strictly applicable to deep donor levels which are greately affected by the chemical shift and valley–orbit splitting. Taking into account only the shallowest donor level and putting the donor binding energy as $E_d = 80(50)$ meV for 6H (4H) [49, 51], we get $a_H = 9(14)$ Å and $n_c = 2 \times 10^{19}$ (5×10^{18}) cm^{-3}, which agrees well with our experimental result.

6.3 Fano interference

Distortion and asymmetry of Raman bands occur when a discrete phonon state overlaps with a broad electronic state and their symmetries coincide with each other [52]. This effect, called Fano interference, was first observed in SiC by Colwell and Klein [32]. The asymmetric profiles vary with the polytype, carrier density and the conduction type (p or n).

As shown in Fig. 8a, the E_2-type FTA bands at ≈150 cm^{-1} in 6H-SiC interfere with a broad valley–orbit transition at low temperatures. On the contrary, this type of interference does not occur in 4H-SiC crystals at carrier density below n_c as seen in Fig. 10a, because these transitions are well separated in energy. However, in more heavily doped samples, which are in the metallic phase, the FTA modes interfere strongly with the electronic continuum extending in the low energy region below about 300 cm^{-1}. These continuum bands may be ascribed to single particle excitations (SPE) of electrons in the conduction band. Since SiC belongs to multivalley semiconductors like Si and Ge, intervally density fluctuations contribute significantly to Raman scattering due to the intervalley density fluctuation mechanism [30]. According to Ipatova's [53] and Cardona's [30] groups, the SPE profile in a collision-limited regime is given by

$$S(\omega) = \left[1 - \exp\left(-\frac{\hbar\omega}{k_B T}\right)\right]^{-1} \frac{\omega A B}{\omega^2 + A^2}\,, \tag{18}$$

where ω is the Raman shift, A is the damping constant, $k_B T$ is the thermal energy, and B is a strength factor determined by the scattering geometry, the effective mass tensor and the density of states of electrons at the Fermi level. It is found that the observed SPE spectra are well described by Eq. (18) [54].

Fig. 16a shows detailed interference profiles of the E_2-FTA bands in 4H-SiC for various carrier densities n. As n increases, the 204 cm^{-1} peak broadens, shifting to lower frequency, and the asymmetry becomes more apparent [35]. We have fitted the well-known Fano profile formula

$$I = \frac{(q + \varepsilon)^2}{1 + \varepsilon^2} \tag{19}$$

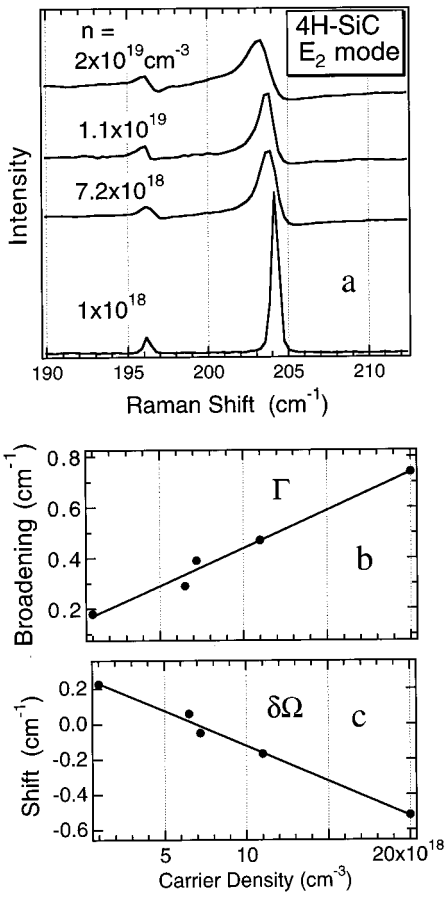

Fig. 16. Fano interference in 4H-SiC for a) different carrier densities; b) broadening and c) shift deduced from the Fano profile fit [39]

to these specta, where q is the asymmetry parameter, and $\varepsilon = (\omega - \Omega - \delta\Omega)/\Gamma$ with ω, Ω, $\delta\Omega$, and Γ being the Raman shift, phonon frequency, peak shift and broadening due to the interference, respectively. Here we used q, $\delta\Omega$, and Γ as adjustable parameters. As shown in Figs. 16b and c, Γ and $\delta\Omega$ vary linearly with n. This result is in accord with the theoretical prediction, indicating that free electrons give dominant contributions to the continuum band. Raman spectra of heavily doped p-type 4H-SiC have also been measured by our group [54]. It is found that a strong continuum band appears extending up to $\approx$1000 cm^{-1}. This band may be due to the intervalence band transitions as reported in p-type Si [55]. The interference features are observed for the TO phonon band at 776 cm^{-1} as well as the FTA phonon bands at $\approx$200 cm^{-1}. These results suggest that the carrier density in heavily doped SiC can be evaluated by analyzing the interference spectra.

References

[1] A. R. Verma and P. Krishna, Polymorphism and Polytypism in Crystals, Wiley, New York 1966.
[2] D. W. Feldman, J. H. Parker, Jr., W. J. Choyke, and L. Patrick, Phys. Rev. **170**, 698 (1968).
[3] D. W. Feldman, J. H. Parker, Jr., W. J. Choyke, and L. Patrick, Phys. Rev. **173**, 787 (1968).
[4] I. S. Gorban and V. I. Lugovoi, Soviet Phys. – Solid State **17**, 1385 (1975).
[5] G. B. Dubrovskii and A. A. Lepneva, Soviet Phys. – Solid State **25**, 1330 (1983).
[6] S. Nakashima, H. Katahama, Y. Nakakura, and A. Mitsuishi, Phys. Rev. B **33**, 5721 (1986).
[7] S. Nakashima, Y. Nakakura, and Z. Inoue, J. Phys. Soc. Japan **56**, 359 (1987).
[8] S. Nakashima, A. Wada, and Z. Inoue, J. Phys. Soc. Japan **56**, 3375 (1987).
[9] S. Nakashima and K. Tahara, Phys. Rev. B **40**, 6339 (1989).
[10] S. Nakashima and K. Tahara, Phys. Rev. B **40**, 6345 (1989).
[11] S. Nakashima, Y. Nakakura, A. Wada, and K. Kunc, J. Phys. Soc. Japan **57**, 3228 (1988).
[12] S. Nakashima and M. Hangyo, Solid State Commun. **80**, 21 (1991).
[13] S. Nakashima, K. Kisoda, and J.-P. Gauthier, J. Appl. Phys. **75**, 5354 (1994).
[14] M. Cardona (Ed.), Light Scattering in Solids I, Springer-Verlag, Berlin/Heidelberg/New York 1983.
[15] S. Nakashima and M. Hangyo, IEEE Quantum Electronics **25**, 965 (1989).

[16] S. NAKASHIMA and H. HARIMA, in: Proc. 6th Internat. Conf. Silicon Carbide and Related Materials, 1995, Ed. S. NAKASHIMA, H. MATSUNAMI, S. YOSHIDA, and H. HARIMA, Institute of Physics Publishing, Bristol 1996 (p. 269).
[17] C. CHENG, K. KUNC, and V. HEINE, Phys. Rev. B **39**, 5892 (1989).
[18] K. KARCH, P. PAVONE, W. WINDL, O. SCHÜTT, and D. STRAUCH, Phys. Rev. B **50**, 17054 (1994).
[19] M. HOFMANN, A. ZYWIETZ, K. KARCH, and F. BECHSTEDT, Phys. Rev. B **50**, 13401 (1994).
[20] R. LOUDON, Adv. Phys. **13**, 423 (1964).
[21] W. WINDL, K. KARCH, P. PAVONE, O. SCHÜTT, D. STRAUCH, W. H. WEBER, K. C. HASS, and L. RIMAI, Phys. Rev. B **49**, 8764 (1994).
[22] S. NAKASHIMA, H. OHTA, M. HANGYO, and B. PALOSZ, Phil. Mag. **B70**, 971 (1994).
[23] D. OLEGO, M. CARDONA, and P. VOGEL, Phys. Rev. B **25**, 3878 (1982).
[24] J. LIU and Y. K. VOHRA, Phys. Rev. Lett. **72**, 4105 (1994).
[25] H. MUKAIDA, H. OKUMURA, J. H. LEE, H. DAIMON, E. SAKUMA, S. MISAWA, K. ENDO, and S. YOSHIDA, J. Appl. Phys. **62**, 254 (1987).
[26] Z. C. FENG, A. J. MASCARENHAS, W. J. CHOYKE, and J. A. POWELL, J. Appl. Phys. **64**, 3176 (1988).
[27] J. F. DIGREGORIO, T. E. FURTAK, and PETROVIC, J. Appl. Phys. **71**, 3524 (1992).
[28] W. S. YOO and H. MATSUNAMI, Japan. J. Appl. Phys. **30**, 545 (1991).
[29] W. S. YOO and H. MATSUNAMI, J. Appl. Phys. **70**, 7124 (1991).
[30] G. ABSTREITER, M. CARDONA, and A. PINCZUK, in: Light Scattering in Solids IV, Ed. M. CARDONA and G. GÜNTHERODT, Springer-Verlag, Berlin/Heidelberg/New York 1984 (p. 5).
[31] M. V. KLEIN, in: Light Scattering in Solids I, Ed. M. CARDONA, Springer-Verlag, Berlin 1983 (p. 147).
[32] P. J. COLWELL and M. V. KLEIN, Phys. Rev. B **6**, 498 (1972).
[33] W. R. LAMBRECHT and B. SEGALL, Phys. Rev. B **52**, R2249 (1995).
[34] P. KÄCKELL, B. WENZIEN, and F. BECHSTEDT, Phys. Rev. B **50**, 10761 (1994).
[35] H. HARIMA, S. NAKASHIMA, and T. HAMAMOTO, in: Proc. 10th Internat. Conf. Raman Spectroscopy, Ed. S. A. ASHER and P. B. STEIN, Wiley, New York 1996 (p. 954).
[36] W. J. CHOYKE and L. PATRICK, Phys. Rev. **127**, 1868 (1962).
[37] YU. A. VAKULENKO, I. S. GORBAN, V. A. GUBANOV, and A. A. PLETYUSHKIN, Soviet Phys. – Solid State **27**, 1342 (1985).
[38] W. J. MOORE, P. J. LIN-CHUNG, J. A. FREITAS, JR., Y. M. ALTAISKII, V. L. ZUEV, and L. M. IVANOVA, Phys. Rev. B **48**, 12289 (1993).
[39] H. HARIMA and S. NAKASHIMA, see [16] (p. 365).
[40] I. S. GORBAN, V. A. GUBANOV, V. D. KULAKOVSKII, A. S. SKIRDA, and B. N. SHEPEL, Soviet Phys. – Solid State **30**, 928 (1988).
[41] YU. N. AZHNYUK, V. V. ARTAMONOV, M. YA. VALAKH, and M. P. LISISTA, Soviet Phys. – Semicond. **20**, 581 (1986).
[42] H. YUGAMI, S. NAKASHIMA, A. MITSUISHI, A. UEMOTO, M. SHIGETA, K. FURUKAWA, A. SUZUKI, and S. NAKAJIMA, J. Appl. Phys. **61**, 354 (1987).
[43] H. HARIMA, S. NAKASHIMA, and T. UEMURA, J. Appl. Phys. **78**, 1996 (1995).
[44] M. V. KLEIN, B. N. GANGULY, and P. J. COLWELL, Phys. Rev. B **6**, 2380 (1972).
[45] G. IRMER, V. V. TOPOROV, B. H. BAIRAMOV, and J. MONECKE, phys. stat. sol. (b) **119**, 595 (1983).
[46] W. L. FAUST and C. H. HENRY, Phys. Rev. Lett. **17**, 1265 (1966).
[47] W. GÖTZ, A. SCHÖNER, G. PENSL, W. SUTTROP, W. J. CHOYKE, R. STEN, and S. LEIBENZEDER, J. Appl. Phys. **73**, 3332 (1993).
[48] S. KARMANN, W. SUTTROP, A. SCHÖNER, M. SCHADT, C. HABERSTROH, F. ENGELBRECHT, R. HELBIG, G. PENSL, R. STEIN, and S. LEIBENZEDAR, J. Appl. Phys. **72**, 5437 (1992).
[49] G. PENSL and W. J. CHOYKE, Physica **185B**, 264 (1993), and references therein.
[50] G. N. VIOLINA, YEH LIANG-HSIU, and G. F. KHOLUYANOV, Soviet Phys. – Solid State **5**, 2500 (1964).
[51] W. SUTTROP, G. PENSL, W. J. CHOYKE, R. STEIN, and S. LEIBENZEDER, J. Appl. Phys. **72**, 3708 (1992).
[52] U. FANO, Phys. Rev. **124**, 1866 (1961).
[53] I. P. IPATOVA, A. V. SUBRASHIEV, and V. A. VOITENKO, Solid State Commun. **37**, 893 (1981).
[54] H. HARIMA and S. NAKASHIMA, unpublished.
[55] F. CERDEIRA, T. A. FJELDLY, and M. CARDONA, Solid State Commun. **13**, 325 (1973).